Bachelor Research Project In Applied Physics

Aerodynamic drag of a model cambered vehicle in asymmetric wind

Author:
I. Soede *(s4385764)*

First examiner:
dr. A. Giuntoli
Second examiner:
prof. dr. ir. P. R. Onck
Daily supervisor:
M. van Beek BSc

February 28, 2023

rijksuniversiteit
groningen

Contents

Acknowledgements

Many regards go out to my colleagues within the Top Dutch Solar Racing team, without them I would not have been able to undertake this project. They have not only offered support through their collective knowledge and sheer motivation but also through incredible friendships. Specifically, I would like to thank my colleagues in the aerodynamics team with whom I have spent many long nights, to create the aerodynamic design of the solar car.

An important thanks go to my supervisors Andrea Giuntoli and Patrick R. Onck, who showed full support of me doing this project in irregular circumstances: outside of an ordinary research group, and before the end of my bachelor's. They have given incredible support, insights, and guidance, that have made this thesis an extremely joyful and educational experience.

1 Introduction

In the last decades, photovoltaic technology has advanced greatly, resulting in higher chances to create a purely solar-powered vehicle. Because of these developments, and the need to explore sustainable energy, the first World Solar Challenge (or WSC) was organized in 1987. The objective of the challenge is to encourage innovation in solar electric vehicle (or SEV) technology by means of an endurance race through Australia. The race starts at Darwin and ends in Adelaide, covering approximately 3200 km. The winner of the challenge is the team that finishes the race the fastest, with an entirely solar-powered vehicle. In this way, the challenge seeks to encourage innovation in SEV technology [1].

The team Top Dutch Solar Racing (or TDSR), situated in Groningen, the Netherlands, has been participating in the challenge since 2019. With their car Green Lightning, they have participated in the WSC and obtained 4^{th} place. In 2021 they participated in the Moroccan World Solar Challenge, an alternative challenge due to the restrictions enforced by the Australian government at that moment, and again obtained 4^{th} place [2].

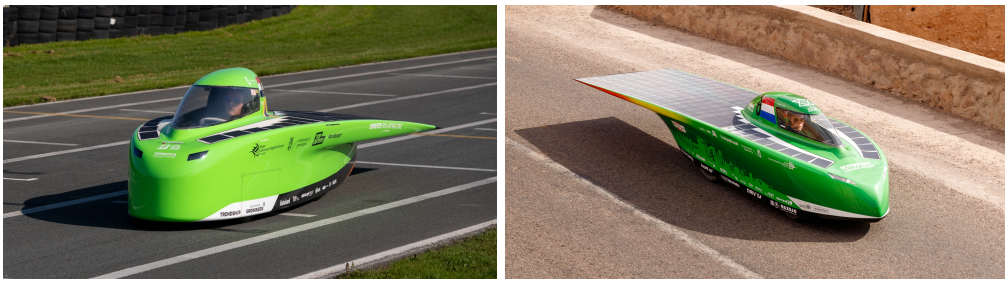

Figure 1.1: The 2019 and 2021 SEVs, Green Lightning (left) and Green Spirit (right), engineered by TDSR. Differences in the cars are not only due to the optimizations but also due to differences in the competition regulations [1].

In the context of SEVs in this challenge, the most significant loss of energy is due to aerodynamic resistance. It is therefore essential that aerodynamic resistance, or drag, is minimized as much as possible to increase the efficiency of the vehicle. Thus far, only the head-on direction of the wind has been taken into account by TDSR when developing the aerodynamic design of the car. This method is time efficient but does not give a complete picture of the aerodynamics in all circumstances. Any side winds will produce an apparent wind that changes the relative velocity magnitude, and more importantly, the relative angle. In fact, the side winds in the race are not symmetrical, so this should be considered and might even be exploited by an asymmetric car design.

In this thesis asymmetry will be introduced by means of cambering the airfoil profile that is used as a basis for SEVs. The expected wind distribution will be derived, which is what the vehicles with varying amounts of camber will then be simulated in. To validate the computational model used for the simulations, a mesh convergence study will be performed. A weighted average of the drag over the probability distribution is then calculated, to determine the effectiveness of cambering the vehicle.

What can be concluded from this computational study is that an increase in cambering causes the weighted drag average to increase. This is because cambering causes a higher drag to be produced then the counteracting lift force, which is explained by the reason that the vehicle cannot be approximated as a simple airfoil. It is however shown that by introducing asymmetry into the vehicle, an asymmetric drag distribution is obtained. With better exploitation of asymmetry into SEVs, an improved weighted drag area could in future research be achieved.

2 Theory

In this section, the theoretical basis for this thesis will be given. The first section is regarding the concept of drag reduction by cambering the vehicle shape, which is the main principle by which asymmetry will be achieved. The latter sections give a basis for the computational model and its methods of validation that will be used.

2.1 Streamlined vehicle aerodynamics

The force at any point on the vehicle is given by the summation of the force perpendicular and tangential to the surface. The perpendicular force is most commonly called pressure force and the tangential force is most commonly called shear force. Integrating the pressure p, and shear stress τ, over the surface S of the car results in the total aerodynamic force on the body, given by the magnitude,

$$F_{aero} = \iint_S p dS + \iint_S \tau dS, \tag{2.1}$$

the component of this force that is opposite to the movement of the vehicle, called drag, is most commonly expressed as follows,

$$F_d = \frac{1}{2} C_d A \rho u_\infty^2, \tag{2.2}$$

where C_d is the drag coefficient, A is a chosen reference area of the vehicle, ρ is the density of the fluid, and u_∞ is free stream velocity. Next to the drag coefficient and reference area, the force is dependent on the velocity and density of the fluid, which does not describe the properties of the vehicle itself. Therefore, the component that can be controlled by the geometry of the car, and should be minimized, is the $C_d A$.

Now consider a situation where the vehicle is moving in a direction and magnitude given by $\mathbf{v}$ and experiences a constant wind parallel to the ground in a frame relative to the ground with magnitude and direction given by $\mathbf{w}$. The apparent wind on the vehicle is then calculated by $\mathbf{w}_a = \mathbf{w} - \mathbf{v}$, see figure 2.1. The apparent angle θ and apparent magnitude w_a are then, by means of the cosine rule, calculated using equation 2.3 and 2.4,

$$w_a = \sqrt{w^2 + v^2 + 2wv\cos\gamma}, \tag{2.3}$$

$$\theta = \arccos\left(\frac{w\cos\gamma + v}{w_a}\right), \tag{2.4}$$

where w and v, are the magnitudes of the previously mentioned vectors, and γ is the angle of the wind $\mathbf{w}$ with respect to the driving direction of the vehicle. In such a situation, the aerodynamic force has a component parallel to the direction of flow, F_d, and a component perpendicular to the flow direction, F_l. This perpendicular force has a great effect on the total drag of the vehicle, which is most easily illustrated in the context of an airfoil as seen in figure 2.1.

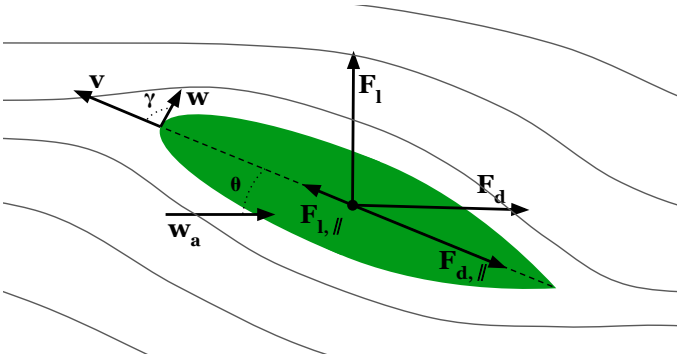

Figure 2.1: Free body diagram of an airfoil at an angle of attack, showing how the total drag force can be reduced by decomposition of the drag and lift force along the chord line (dashed line). The airfoil can be interpreted as an SEV in the top view.

The airfoil produces an upwards force F_l, called lift, and a backwards force F_d, called drag. When breaking these forces down in the direction of the chord line, that is the line connecting the leading and trailing edge of the airfoil, the lift force produces a component opposite to the drag force. The total force in the direction of the chord line is expressed by equation 2.7.

$$F_{tot,\parallel} = F_{d,\parallel} - F_{l,\parallel}, \tag{2.5}$$

$$= F_d \cos\theta - F_l \sin\theta, \tag{2.6}$$

$$= \frac{1}{2}\rho A w_a^2 (C_d(\theta)\cos\theta - C_l(\theta)\sin\theta), \tag{2.7}$$

this breaking down of forces has the important conclusion that an airfoil that produces lift at an angle of attack can have a reduced drag in the direction of the velocity vector $\mathbf{v}$ or the chord line) compared to an airfoil that produces less lift but the same drag at that same angle, assuming that the drag increases minimally. In the context of an SEV, where the driving direction is the chord line, the drag can be reduced by creating 'lift'. This effect is very significantly seen in for example a sailboat, where the sail produces a force that can propel the boat forwards. Because we are dealing with an asymmetric distribution of side winds, the weighted average drag can be calculated according to equation 2.8, which assumes a constant wind velocity,

$$\overline{C_d A} = \frac{2}{\rho w_a^2} \int P(\theta) F_d(\theta) d\theta, \tag{2.8}$$

where $P(\theta)$ gives the probability of an apparent wind happening at θ. To simplify notation, F_d is now the drag in direction of the chord line $F_{tot,\parallel}$, instead of in the direction of the wind. The way by which lift at angles of attack can be manipulated in airfoils is by means of cambering, which is the asymmetry of an airfoil along the chord line. The camber line is the collection of points equidistant from the bottom to the top surface of the airfoil. The maximum camber is a percentage of the maximum distance from the chord to the camber line with respect to the chord length. In figure 2.2 two similar 4-digit NACA airfoils can be seen, one symmetric, and one cambered with 1% maximum camber [3].

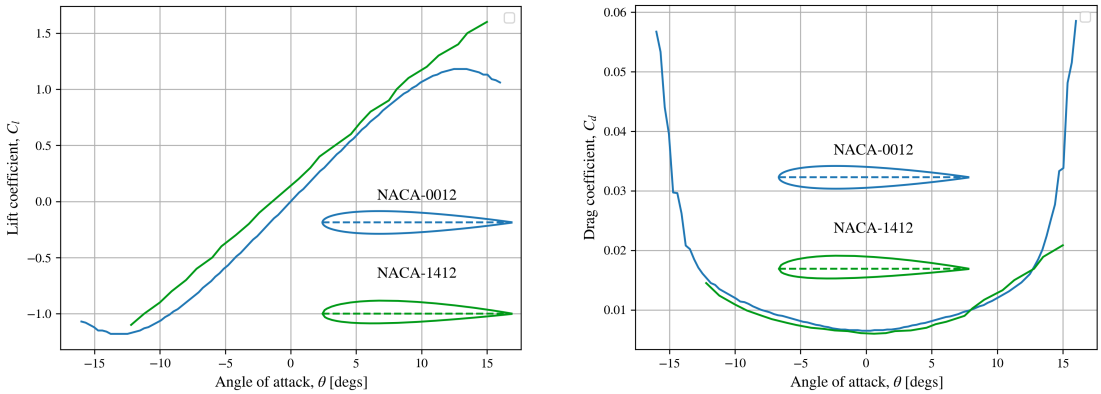

Figure 2.2: Lift constant versus angle of attack for a symmetric and cambered airfoil: NACA-0012 (max thickness 12% of the chord at 30% chord) and NACA-1412 (max thickness 12% of the chord at 29.9% chord and maximum camber 1% at 40% chord) respectively [4][5].

What can be seen from the figure is that the lift profile is significantly different for the symmetric airfoil. The point at which the cambered airfoil generates 0 lift has shifted to a negative angle of attack compared to the symmetric airfoil. Meaning that before this point the cambered airfoil will not help in reducing the drag in the direction of the chord line. But after this point, the cambered airfoil could help more than the symmetric airfoil. This is assuming that the drag force does not increase significantly when cambering the airfoil, which is the case for this situation as can be concluded from figure 2.2. Finding the optimal cambered airfoil profile to minimize the amount of drag in a side wind distribution has therefore become a complicated task, which is the subject of this thesis [6].

2.2 Turbulence model

A viscous fluid flow is governed by the Navier-Stokes (or N-S) equations. Solving these directly using direct numerical simulation requires a very fine spatial and temporal resolution to resolve the turbulent effects on all scales. On a large scale with high Reynolds numbers, this is computationally too expensive. Instead, an approximate model of turbulence will have to be used. In the following section the approximations to the turbulence model that will be used, the $k-\omega$ Shear Stress Transport (or SST) model, are derived and motivated.

In a model where flow is incompressible and without external body forces the N-S equations reduce to the following equations.

$$\rho\frac{Du_i}{Dt} = -\frac{\partial p}{\partial x_i} + \mu\frac{\partial^2 u_i}{\partial x_j \partial x_j}, \tag{2.9}$$

$$\frac{\partial u_i}{\partial x_i} = 0, \tag{2.10}$$

where u_i is the flow velocity, $\frac{Du_i}{Dt} = \frac{\partial u_i}{\partial t} + u_j\frac{u_i}{x_j}$ is the material derivative of the flow velocity, p is the pressure, μ is the dynamic viscosity, and ρ is the density. Using Reynolds decomposition, the dependent flow variables are separated into a mean, temporally and spatially independent part, and a fluctuating, temporally and spatially dependent part [7].

$$u_i = \overline{u_i} + u_i', \tag{2.11}$$

$$p = \overline{p} + p', \tag{2.12}$$

the average of the fluctuating part reduces to zero when averaging. Using the conventional ensemble rules of averaging the Reynolds Averaged N-S equations, or RANS equations, it follows that,

$$\rho\frac{D\overline{u_i}}{Dt} = -\frac{\partial\overline{p}}{\partial x_i} + \mu\frac{\partial^2\overline{u_i}}{\partial x_j\partial x_j} + \frac{\partial}{\partial x_j}R_{ij}, \tag{2.13}$$

$$\frac{\partial\overline{u_i}}{\partial x_i} = 0, \tag{2.14}$$

where $R_{ij} = -\rho\overline{u_i'u_j'}$ are the Reynolds stresses. By expressing the Reynolds stresses in terms of the mean flow variables, the RANS equations can be solved. In the eddy viscosity model this is done by means of the Boussinesq hypothesis [8], which assumes that turbulence is due to Brownian motion and introduces a new variable μ_t, called the eddy viscosity,

$$R_{ij} = 2\mu_t S_{ij}^* - \frac{2}{3}k\delta_{ij}, \tag{2.15}$$

where $S^{ij} = \frac{1}{2}\left(\frac{\partial\overline{u_i}}{\partial x_j} + \frac{\partial\overline{u_j}}{\partial x_i}\right)$ is the strain rate, $k = \frac{1}{2}\rho\overline{u_i'u_i'}$ is the turbulent kinetic energy, and δ_{ij} is the Kronecker delta. The Eddy viscosity, μ_t, is then modeled by the two-equation turbulence model $k-\omega$ SST introduced by Wilcox [9],

$$\mu_t = \frac{k}{\omega}, \tag{2.16}$$

where ω is the specific turbulence dissipation rate. This results in the following equations for the $k-\omega$ SST model [9],

$$\frac{\partial k}{\partial t} + u_j\frac{\partial k}{\partial x_j} = R_{ij}\frac{\partial u_i}{\partial x_j} - \beta^* k\omega + \frac{\partial}{\partial x_j}\left[\left(\mu + \sigma^*\mu_t\right)\frac{\partial k}{\partial x_j}\right], \tag{2.17}$$

$$\frac{\partial \omega}{\partial t} + u_j\frac{\partial \omega}{\partial x_j} = \alpha\frac{\omega}{k}R_{ij}\frac{\partial u_i}{\partial x_j} - \beta\omega^2 + \frac{\partial}{\partial x_j}\left[\left(\mu + \sigma\mu_t\right)\frac{\partial \omega}{\partial x_j}\right], \tag{2.18}$$

where the coefficients α, β, β^*, σ and σ^* can be found at [10]. This results in the following approximations being used for the $k-\omega$ SST model:

- The fluid is incompressible and without body accelerations.
- The Boussinesq hypothesis holds, meaning that turbulence is approximated as Brownian motion. There are no impinging jets, strong curvatures, and axial strains present in the geometry [11].

To find the drag forces, first equations 2.18 and 2.19 are simultaneously solved, after which a velocity and pressure field is known. Then the shear stress on the surface of the vehicle can be calculated by taking the derivative of the velocity with respect to the distance to the surface. Together with the pressure on the surface of the vehicle, the total force can be calculated according to equation 2.1. The software that will be used to perform the simulations is Ansys Fluent 2022 R2 [12], which uses the Finite Volume Method to discretize the equations used in the $k-\omega$ SST model and the SIMPLEC algorithm to solve the equations.

2.3 Fluid boundary layer

In viscous fluids, the no-slip condition states that due to adhesive forces between the fluid and solid boundary, the fluid has zero velocity at the solid boundary. Due to cohesive forces within the fluid, the velocity of the fluid from that boundary gradually approaches the free stream velocity. This forms a layer of flow close to the solid surface, called a boundary layer. The

average velocity profile of a boundary layer can be expressed in terms of y^+ and u^+ [13]. Here y^+ is the dimensionless distance to the no-slip surface,

$$y^+ = \frac{yu_\tau}{\nu}, \tag{2.19}$$

where $u_\tau = \sqrt{\frac{\tau}{\rho}}$, y is the distance to the surface, and ν is the kinematic viscosity of the fluid. The dimensionless velocity at the dimensionless distance to the surface is given by,

$$u^+ = \begin{cases} y^+ & y^+ < 5 \\ \frac{1}{\kappa} \ln y^+ + C^+ & y^+ > 30 \end{cases},$$

where for smooth walls, the von Karman constant $\kappa \approx 0.41$ and $C^+ \approx 5.0$ [13]. The region between 5 and 30 y^+ is not approximated by a linear or logarithmic law. Because the $k-\omega$ SST model does not approximate the boundary layer, it has to be discretized entirely. Therefore it is important that the element size close to the wall is valued multiple times smaller than 5, such that the entire velocity profile is captured. In section 4.1.3 it will be shown that this is indeed the case.

2.4 Richardson extrapolation

The issue with discretizing (or meshing) the computational domain is that the discretization (or mesh) has to be fine enough to capture the flow variable gradients, but coarse enough to not be too computationally expensive. A finer mesh will always produce a more accurate result, that will approach the true value with an infinitely fine mesh. The purpose of this section is to motivate the chosen mesh size based on accuracy and computational costs and to determine an approximate error of the mesh using Richardson extrapolation. This method is presented in the book by Roach [14].

Suppose we have a number of different meshes that each have a different mesh size h. After running the simulations they produce a result $f(h)$, which is assumed to be determined entirely by the discretization of the domain. Assuming the results are in the asymptotic region, the results get more accurate as h approaches 0. The result can be approximated in the following manner [15],

$$f = f_{h\to 0} + c_1 h + c_2 h^2 + \ldots, \tag{2.20}$$

if the solution is order p, that means constants c_1 untill c_{p-1} are all 0. Then for a constant refinement ratio r, the limit can be approximated as follows,

$$f_{h\to 0} \approx f_1 + \frac{f_1 - f_2}{r^p - 1}, \quad \text{where } p = \ln(\frac{f_3 - f_2}{f_2 - f_1}) / \ln(r), \tag{2.21}$$

where f_1, f_2, f_3 are the results from mesh sizes h_1, h_2, h_3, organised from coarse to fine. Then according to Roach, the fractional error of spacing h_1, h_2 are given by,

$$E_1 = \frac{\varepsilon}{r^p - 1}, \quad E_2 = \frac{\varepsilon r^p}{r^p - 1}, \tag{2.22}$$

where ε is the relative error defined to be $\frac{f_2 - f_1}{f_1}$. These errors can then be applied to the measured information on which the study was performed, which in this case is the drag force on the model. This information can then be used to decide which mesh to use to get an optimal balance of computational efficiency and model accuracy.

3 Methods and model setup

In this section, the steps taken to set up the computational fluid dynamics (or CFD) model are explained. This involves the simplification of the vehicle geometry, then discretizing the domain (or meshing) by specifying the size of the discretization elements, and last, determining the boundary conditions of the model. Next to that, the amount of camber in the vehicles will be motivated, the setup of the high-performance cluster (or HPC) will be shown, and the approach to the mesh convergence study will be explained.

3.1 Geometry simplification

Simulating a completely realistic model computer-aided design (or CAD) model, where every feature is resolved, is not viable because of increasing complexity when discretizing the domain and because of an increase in computational time to resolve every feature. In the following points, the simplifications that are made to the model geometry are explained.

- To allow for the better discretization of the fluid at the contact between wheels and ground, so-called patches are added, which can be seen in figure 3.1. These patches allow for larger mesh sizes to be used as the infinitely narrow space at the contact line between wheels and the ground does not need to be meshed.

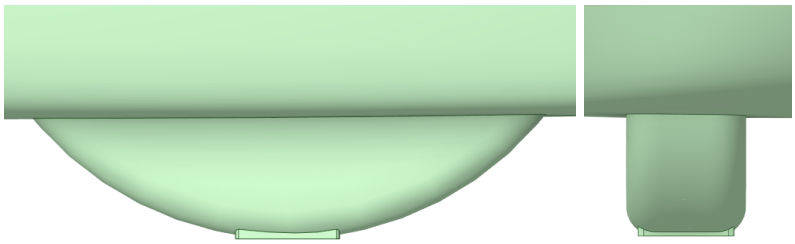

Figure 3.1: Front and side view of wheel patches. Their size has been kept minimal to not interfere with fluid flow.

- The trailing edge of the vehicle has a thickness of 1.5mm, this has been increased to 4.5mm to allow for better discretization with larger elements.
- Because of material roughness, component and material junctions, and manufacturing imperfections, the surface of the vehicle is not always hydraulically smooth. It is assumed in this model that the geometry everywhere is perfectly smooth.
- Due to suspension travel and steering movement of the wheels, there needs to be some clearance to prevent the wheels from touching the body. This clearance creates a hole in the body through which air can flow. Because modeling the insides of the car makes the model too complex, the model is not designed with any clearance around the wheels.
- To improve aerodynamic efficiency, the wheels are enclosed by shells approximately 10 mm removed from the wheels which can be seen in figure 3.2. Because the insides of the vehicle are not modeled, this feature is not included in the simulation.

Figure 3.2: The wheel shell that is located around a majority of the wheel. This relatively complicated part will not be simulated.

3.2 Mesh generation

The next step is to determine how finely discretized different regions of the computational should be. In regions where high-velocity gradients are expected, the fluid should be finely discretized. In regions where low-velocity gradients are expected, the fluid can be coarsely discretized. In the following points from fine to coarse, the refinements in the computational domain will be motivated.

- In this model a boundary layer is expected on every surface where there is a movement of the fluid relative to a surface, which includes the solar car, the wheels, and wheel patches. As described in section 2.3, to fully resolve the boundary layer, the first cell layer height is of great importance. For these simulations that height will be $1 \cdot 10^{-5}$m, which will be more thoroughly motivated in section 4.1.3.
- In regions where the model has extreme curvatures, such as the wheels, canopy trailing edge, and vehicle trailing edge, large adverse pressure gradients $\frac{dp}{dx} > 0$ can cause the flow to recirculate. This may result in flow separation and turbulence, which can greatly increase the drag on the vehicle [16]. To be able to capture the effects of flow separation and the wake on the vehicle, the mesh is refined in regions where this is predicted to happen. These volumes of refinement or so-called bodies of influence (or BOIs) are visualized in figure 3.3.

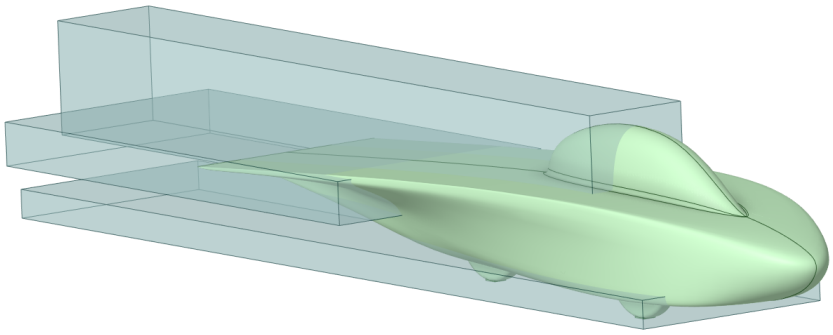

Figure 3.3: Placement of BOIs where separation of attached flow may happen: at the wheels, near the end of the canopy, and at the vehicle trailing edge.

- Due to the viscosity of the fluid, far away from the surface of the SEV the fluid flow approaches the free stream velocity direction and magnitude. In this region the velocity gradients are very small, therefore a large mesh size can be used. In figure 3.6 can be seen how three BOIs are used to create a transition from a region near the vehicle, to far away from the vehicle.

To simulate an angle of attack, all objects in the computational domain, except the vehicle with the nearest refinement BOI, are rotated with respect to the origin. An example of which can be seen in figure 3.4.

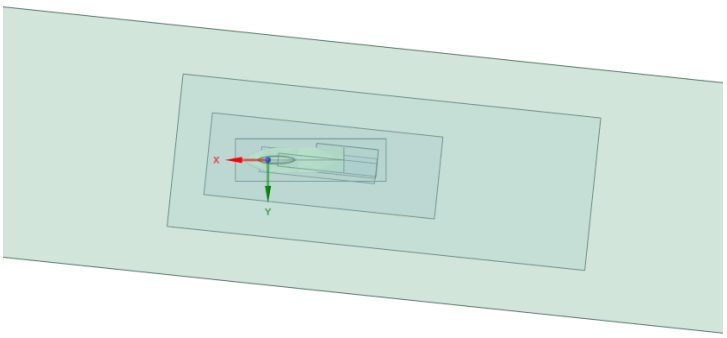

Figure 3.4: Rotation of objects in the computational domain to obtain apparent wind for the symmetric vehicle at a 6 degrees angle of attack. The origin does not change its orientation, the x direction is always in line with the driving direction of the vehicle.

In table 3.1 the sizing used on each fluid domain component are listed. A sizing determines the element size of that object. The sizings are motivated by the mesh convergence study, of which more information can be found in section 2.4, 3.6 and 4.1.2.

Object	Geometry type	Mesh size
trailing edge	edge	1 mm
wheel patches	face	2 mm
SEV body and wheels	face	7 mm
BOI wakes	body	15 mm
BOI near	body	5 cm
BOI middle	body	20 cm
BOI far	body	30 cm
enclosure	body	51.2 cm

Table 3.1: Mesh sizings for every object in the computational domain. Showing that farther from the vehicle, discretization elements are significantly larger.

Using this information Ansys Fluent Meshing 2022 R2 meshes the geometry, which uses a non-structured, poly-hexcore mesh. Meaning that close to surfaces it will use a polygonal mesh to better capture the geometry, and far away from the surface it uses a hexagonal mesh for increased computational performance [17]. The resulting mesh can be seen in figure 3.5.

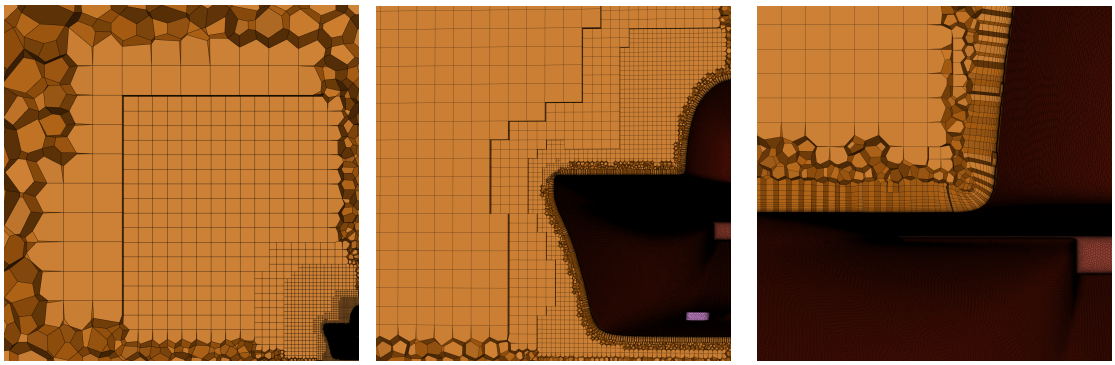

(a) (b) (c)

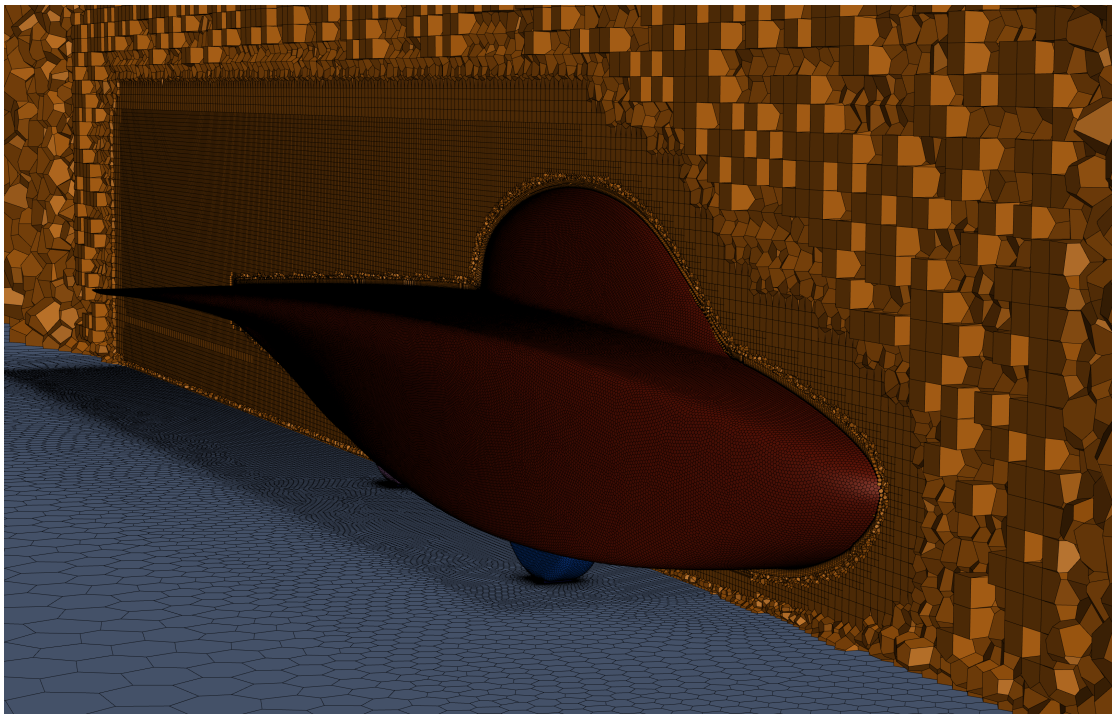

(d)

Figure 3.5: In images a, b, and c a cross-section of a plane perpendicular to the driving direction can be seen, from the large enclosure-sized elements in c to the extremely fine boundary layer elements in a. In image d, a perspective view of the meshed car geometry and its near surroundings.

3.3 Boundary conditions

In figure 3.6, the boundary conditions used for the setup can be seen. Five car lengths in front of the vehicle, there is a velocity inlet, which lets an airflow into the domain at 25 m/s perpendicular to the inlet surface. Fifteen car lengths behind the vehicle, there is a pressure outlet, which defines an outflow condition based on pressure [18]. The domains sides and top consist of symmetry surfaces, meaning that the no-slip condition is not applied to them. The ground, together with the car body, wheels, and patches do have a no-slip condition. The ground and wheels have moved relative to the vehicle, which is modeled using the moving reference frame method. The ground has a velocity of 25 m/s with respect to the car, and the wheels have a velocity of 92.59 rad/s with respect to the car. In section 4.1, these values will be motivated more thoroughly. The density of the fluid is 1.255 kg/m^3 and the viscosity of the fluid is

$1.7894 \cdot 10^{-05} kg/(m \cdot s)$[19].

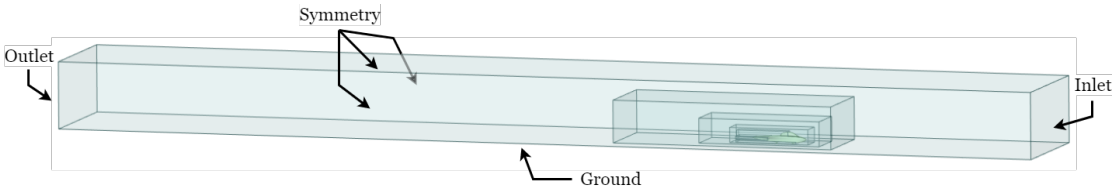

Figure 3.6: Enclosure geometry with refinement objects and boundary conditions. The size of the enclosure is approximately 100x13x7 meters.

3.4 Cambered vehicles and apparent wind angles

The method by which cambering will be applied in this thesis is by moving the leading and trailing edge of the SEV. This in turn moves the chord line of the vehicle. Then, by keeping the widest part of the airfoil consistent among all vehicles, the amount of maximum camber is the amount we have moved the chord line. The location of maximum thickness of the airfoil is located at the wheels. The reason for this method is to not increase the width of the vehicle which significantly increases the aerodynamic drag of the vehicle. The models will be made in the CAD software Rhinoceros 3D [20] by my colleague Ayzo Wiertsema.

The SEV model that is taken for this thesis is the SEV designed by TDSR for the 2023 WSC. Because the optimum amount of camber is unknown, a wide range of camber has been taken: 0mm (symmetric), 25mm, 50mm, 100mm, and 150mm. At a 150mm camber, it becomes unrealistic to produce the model geometry. The camber has been chosen to be directed to the right, compared to the driving direction, such that lift is maximum when there is a wind from the left (the most prevalent direction as shown in figure 4.1). In this case, the maximum camber is measured in millimeters. In the context of airfoils, it is conventional to express it as a percentage of the chord line. This conversion is made by dividing the maximum camber by the length of the vehicle, which is 5 meters, and multiplying by 100%. Converting the mm values to percent gives a maximum camber of 0.5%, 1%, 2%, and 3% camber located at 23.2% of the chord. This is the convention that will be used from now on. The application of this can be seen in figure 3.7.

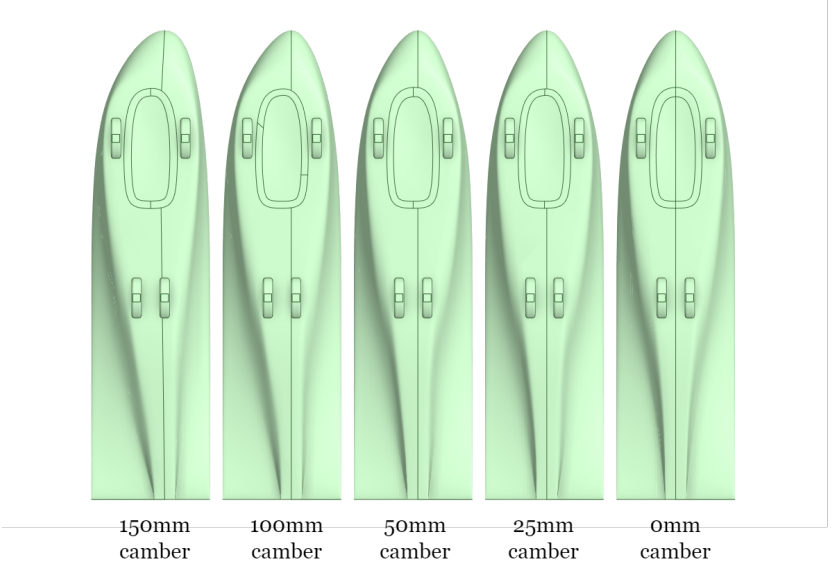

Figure 3.7: Bottom view of every vehicle, showing how the airfoil profile changes but the vehicle thickness remains the same as camber is introduced into the vehicle.

These vehicles will each be simulated at -6, -4, -2, 0, 2, 4, and 6 degrees angle of attack, where a negative angle is to the left of the driving direction and a positive angle is to the right of the driving direction. These angles cover almost the entire distribution of apparent winds that can be found during the race, which will be shown in 4.1. A weighted average drag area will then be calculated using the probabilities of the distribution as weights, to obtain a value that represents the average performance of the vehicle during the race. Plotting the weighted average drag area versus the amount of camber should then reveal whether camber can improve performance.

3.5 Cluster configuration

The 35 simulations were run on Peregrine, the HPC of the University of Groningen. For every simulation, 48 cores and 60 gigabytes of RAM were requested. On average the simulations ran 12.52 hours per simulation. Running in parallel the simulation took approximately 4 days to complete.

3.6 Mesh convergence study

To determine the optimal mesh size a mesh convergence study is performed. The study takes multiple steps to refine the mesh used for the simulation, to then look at the result of each mesh to determine which mesh can be used to produce an accurate result.

For the mesh convergence study the same computational setup will be used as described in the previous sections. The only difference is that just the half-domain case of the 0% camber car is simulated since this is done to save computational time. The mesh will be refined in 3 steps, with a refinement factor of 1.2. The sizings are given by table 3.2. An error can then be calculated on the simulations according to the equations in section 2.4.

Object	h_1	h_2	h_3
SEV body and wheels	8.4 mm	7 mm	5.83 mm
BOI wakes	18 mm	15 mm	12.5 mm
BOI near	6 cm	5 cm	4.17 cm
BOI middle	24 cm	20 cm	16.67 cm
BOI far	36 cm	30 cm	20.83 cm

Table 3.2: Steps of refinement for the mesh convergence study. Unmentioned sizings remain constant and are mentioned in section 3.2.

To get accurate errors on the measurements the study should be done for every vehicle and angle, this would however multiply the required amount of simulations by threefold. We, therefore, assume that the result of the 0 degrees, 0% camber case, can be extrapolated to all the other cases.

4 Results

In this section, the results of the main research will be shown and discussed. Next to that, the preliminary results will be shown, this includes the derivation of the wind distribution, the grid convergence study, and quality metrics of the CFD simulation.

4.1 Preliminary results

4.1.1 Analysis of race wind distribution

As stated before in previous sections, the wind distribution during the race is asymmetric, meaning that winds are more likely to come from one direction than another. As this statement is the motivator for this thesis, in the next section we will show why this statement is true and show that it is valid to assume this for the next races.

To make a distribution of winds, data was taken at 102 points along the course from weather stations from the meteorology service company, Meteoblue [21]. To create a more generalized distribution, the time period of the data has been extended to a week before and after the race, going from 16$^{\text{th}}$ of October to the 3$^{\text{rd}}$ of November. This is assuming that the weather does not significantly change over this time period. This period has been taken from years from 2000 to 2019. The positions at which measurements have been taken and the resulting distribution can be seen in figure 4.1.

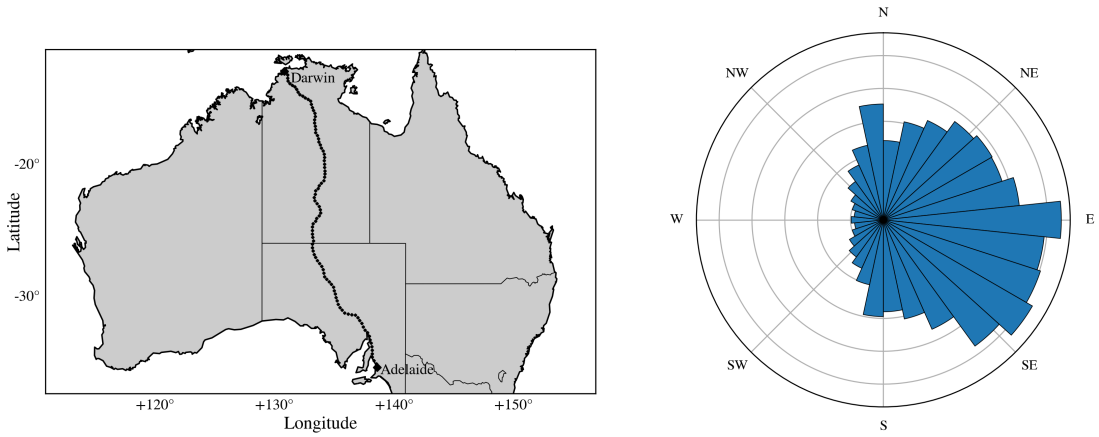

(a) Mercator projection of Australia showing the points along the course at which weather data was taken. The driving direction is from north to south.

(b) The wind distribution relative to geographic north.

Figure 4.1: The datapoints and its distribution from which can be concluded that winds are more probable to come from the east than from the west.

As can be seen from the graph, winds are significantly more likely to come from the east as opposed to the west. The average of the distribution is 147.62 degrees. The standard deviation of the average of each year's data calculates to be 14.57 degrees, revealing that the average remains relatively consistent. The standard deviation of the standard deviation of every year is 8.98 degrees, confirming that the shape of the distributions is also consistent over the years. This gives good reason to assume that in the next years, a similar, asymmetric distribution, can be expected.

Another important consideration to take into account is whether the wind speed remains constant among the angles of attack. If this is not the case then this should be considered into account, since a significant change in velocity also has a significant change in force on the vehicle. The distribution of velocities for 40-degree intervals of the distribution of figure 4.1b can be seen

in figure 4.2. Here the average of all the data is 3.85 m/s, around which every distribution is approximately centered. We can therefore assume a constant wind speed for all angles of attack.

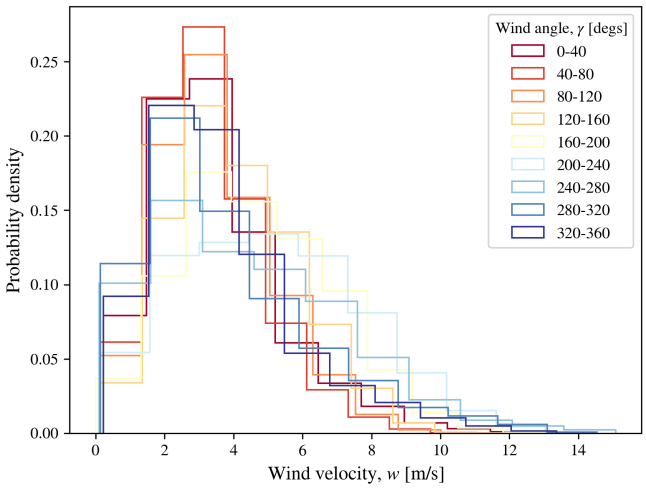

Figure 4.2: Wind velocity distributions of different bins of wind angles. Because all these distributions are similar, for every apparent wind angle, the same wind velocity can be expected.

These are however not the apparent winds we are interested in. Assuming we drive an average of 25 m/s the apparent wind angle distribution can be calculated from equation 2.4 and can be seen in figure 4.3. Because the tails of the distribution account for a small total probability of 3%, they will be ignored for the remainder of this research. Ignoring these angles will result in fewer simulations to be run to capture the distribution, for calculating the weighted average, the probabilities of the used angles will be normalized to 1, which can be seen in table 4.1.

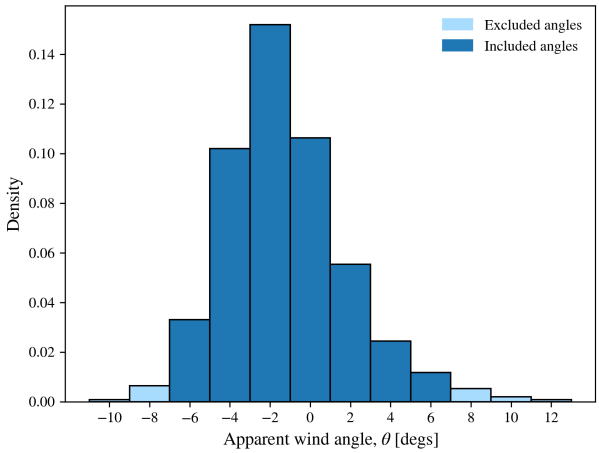

Figure 4.3: The apparent wind distribution for a vehicle velocity of 25 m/s. The degrees that are not included in the experiment are shown with a lighter shade, this is 3% of the total distribution.

θ	$P(\theta)$
-6	0.0682
-4	0.210
-2	0.313
0	0.219
2	0.114
4	0.0504
6	0.0243

Table 4.1: Normalized probability factors that will be used to calculate the weighted drag average.

4.1.2 Mesh convergence study

The result of the convergence study can be seen in table 4.2, and plotted in figure 4.4. The results of the experiment are given in blue, and the extrapolation is given in orange. The errors calculated per spacing are applied to the point in the graph.

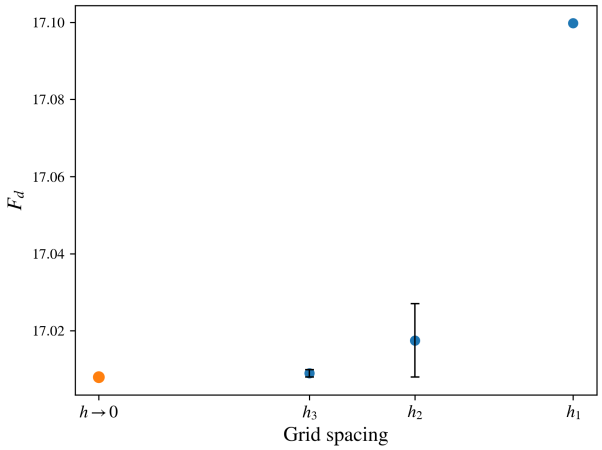

Figure 4.4: Richardson extrapolation was performed on 3 instances of mesh refinement. With a finer grid spacing the true value is approximated.

Grid spacing, h	Drag F_d [N]
h_1	17.100
h_2	17.017
h_3	17.009
$h_{h\to 0}$	17.008

Table 4.2: Results of the mesh independence study, together with the Richardson extrapolation calculated from the results.

As by the theory in section 3.2, the relative error of spacing h_2 is calculated to be 0.056%, and for spacing h_3 it is calculated to be 0.006%. This gives enough reason to use the coarser mesh, as it results in an error that is likely fine enough to observe no difference.

4.1.3 CFD quality metrics

Boundary layer y^+

As discussed in section 2.3, the discretization of the boundary layer is of great importance. In section 3.2 the first cell height in the boundary layer was chosen. It will quickly be shown that this height did indeed produce the right value of y^+. From figure 4.5 a contour plot of the y^+ of the first cell layer on the vehicle's surface can be seen. This is taken from the same mesh convergence study, of this grid spacing that will be used for the remainder of this research. The y^+ value does not exceed 1.1 anywhere on the surface and is centered below 1, which means the boundary layer is resolved very well to capture the viscous and non-viscous sub-layers.

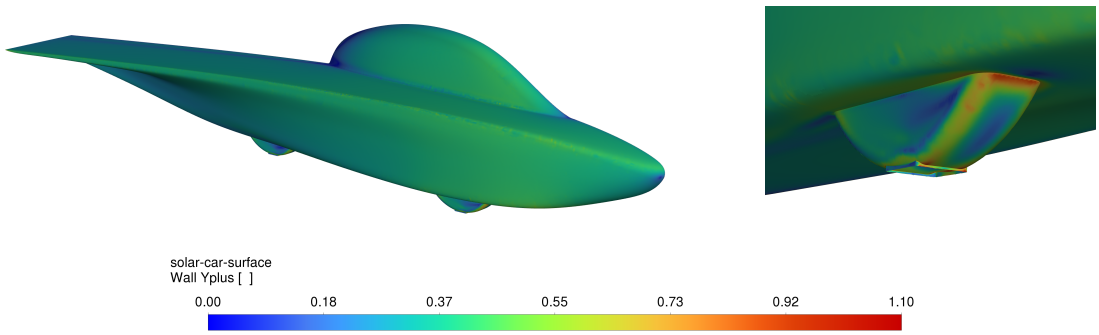

Figure 4.5: Contour plot of the y^+ value on the surface of the vehicle. A higher y^+ means a lower discretization of the boundary layer. Everywhere on the vehicle the y^+ is small enough.

Mass imbalance
The mass imbalance is the deviation of mass flow measured at the outlet compared to the inlet. If it is substantial it means that there is not as much mass going into the simulation as out of the simulation, which is not possible because density is assumed to be constant throughout the domain. This is an indication that the simulation is incorrect. The average percentual mass flow difference on all simulations is $(4.44 \pm 12.57) \cdot 10^{-7}$ %. This is no reason for concern.

4.2 (Non)cambered vehicles

The collection of all drag area values at the simulated angles of attack can be seen in figure 4.6.

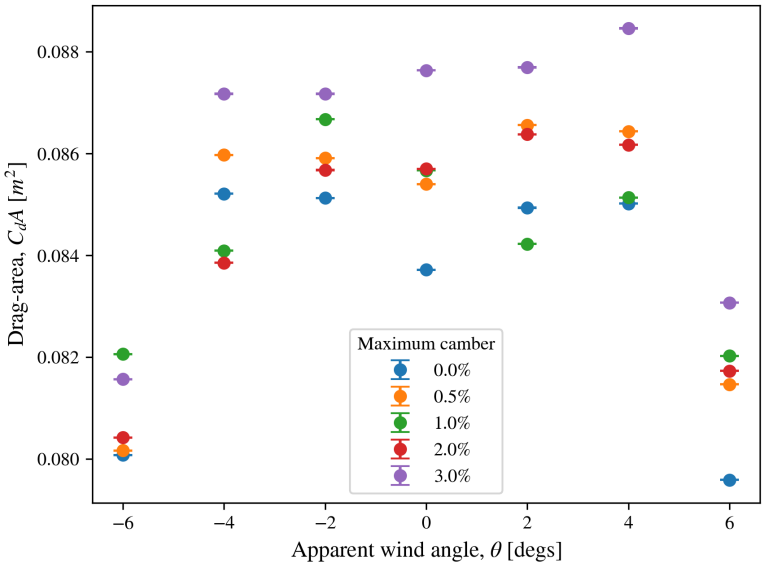

Figure 4.6: Drag area distribution for all vehicles. The distribution for cambered vehicles is clearly asymmetric, where the symmetric vehicle's distribution is mostly symmetric.

What can be seen is that most vehicles do not have a single point of minimum drag, but rather a single point of maximum drag. A peculiarity can be seen in the 0% camber case, where the vehicle has two maxima instead of one. As expected the distribution for asymmetric vehicles is indeed asymmetric, whereas the symmetric case is symmetric to an extent, the forces at negative angles of attack are not the same as the forces at the respective positive angles of attack. This reason is likely due to asymmetry in the mesh itself. This error does not however lie within the previously determined error margins.

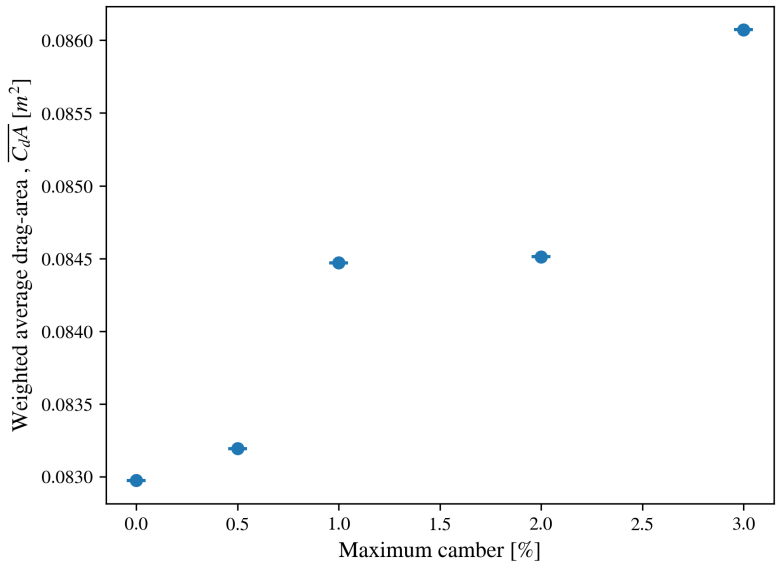

Figure 4.7: An increase of the weighted drag average can be observed when increasing the amount of maximum camber. This has the conclusion that camber negatively affects the vehicles aerodynamics during the race.

Taking the weighted average, using the distribution found in 4.1.1, we can find how the performance of the vehicle changes as the amount of camber is increased. The result can be seen in figure 4.7. The weighted drag area increases with the amount of camber, which is in contradiction with the initial hypothesis. It was expected that there would be an optimum camber, that would be below the drag of the symmetric vehicle. The reason for this can be explained when looking at the following graphs.

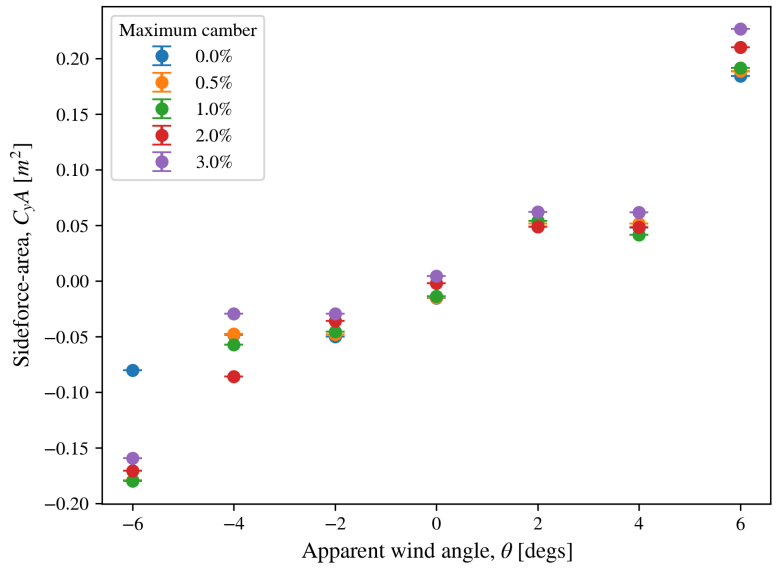

Figure 4.8: Side wards force distribution for all vehicles. In general, the distributions are very similar, with cambered vehicles having a slightly higher value.

In figure 4.8 the side force across the distribution for all vehicles can be seen. If the asymmetric vehicles were to produce a significant amount of lift, then they are expected to produce a clear asymmetric distribution of side forces, this is not the case. It is true that in general, the 3%

camber data points seem to be above the 0% data points, showing some asymmetry in the distribution similar to figure 2.2. At -6 degrees, 0% camber, the measured value is out of line with the trend, the reason for this is unclear. At 0 degrees angle of attack, the asymmetric vehicles are expected to produce a side force that increases with camber. In figure 4.9 the side force at 0 degrees versus the amount of camber can be seen.

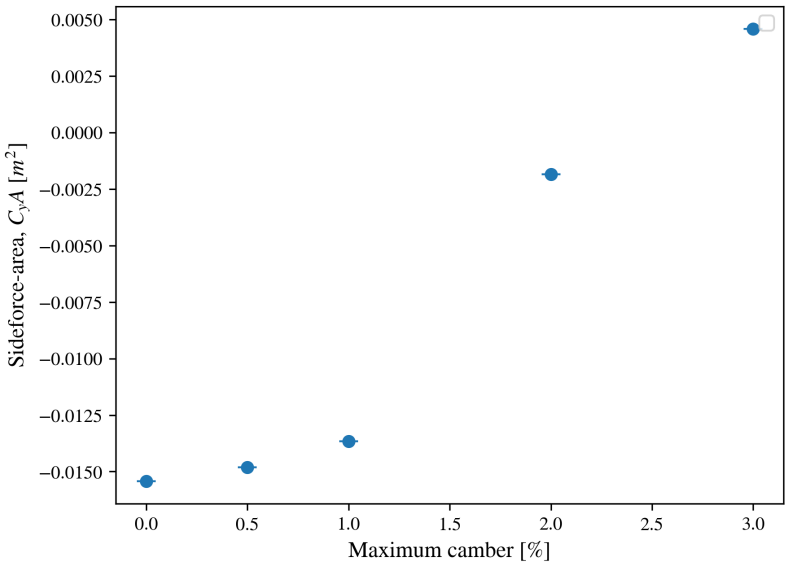

Figure 4.9: Sidewards force at 0 degrees for all cambered vehicles, showing that a side wards force increases with the amount of camber.

From this figure it is clear that it is indeed the case that there is a correlation between the side force and camber. This shows that the cambered vehicles do produce a drag-reducing force to some extent. However, it seems that the effect of camber has a negative effect on the drag of the vehicle. The initial assumption that the drag would change minimally with the amount of camber is therefore wrong. It increases more than the drag-reducing force, which in total increases the drag of a cambered vehicle. To confirm whether the body of the vehicle behaves like an airfoil we can look at the pressure along a line on the airfoil-shaped part of the vehicle. An airfoil that produces lift will have a higher pressure on one side of the airfoil compared to the other [16].

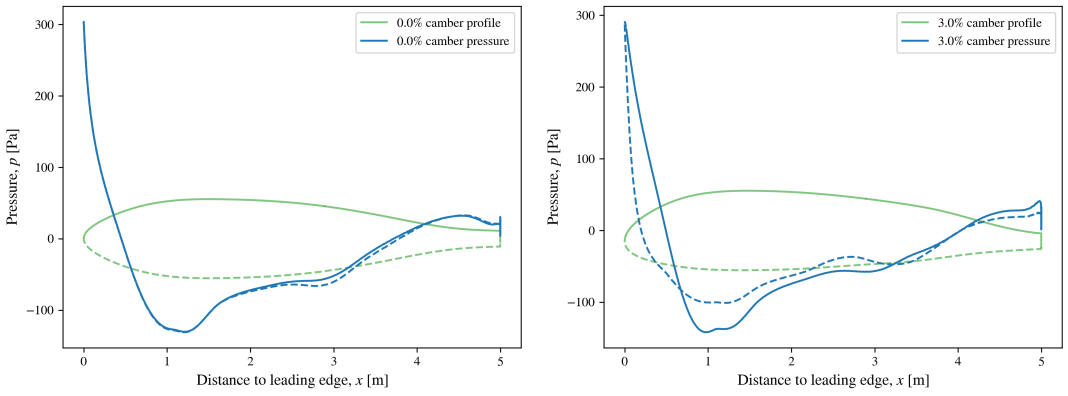

(a) 0% camber

(b) 3% camber

Figure 4.10: Static pressure along the sides of the car, for both the symmetric and most cambered vehicle. In the cambered case, the net pressure is approximately 0.

The result can be seen in 4.10. The line along which the pressure has been measured can be seen in green in the plot. This line is the intersection with a plane parallel to the ground at 0.38m high, intersecting with the leading and trailing edges. Even though the pressure profile at the top of the airfoil is different from the bottom profile, what can be seen is that in both cases there is barely a net positive (or negative) pressure difference between the top and bottom line. Therefore the model does not work as efficiently in creating lift as a simple airfoil, and cannot be approximated as such.

5 Conclusion

From the figure 4.7 it can be concluded that as the maximum camber increased, the weighted average drag area also increases. This means that the method of cambering as described in this thesis on the 2023 SEV model created by TDSR does not increase aerodynamic performance when considering an asymmetric wind distribution. The reason for this can be concluded from figure 4.8 and 4.9, where even though the cambered vehicle generates a small side force, it is not enough to overcome the increase of drag that is created when cambering the vehicle. From 4.10 we can see that on the airfoil section of the vehicle, there is not a significant pressure difference between either side, which means that the airfoil section of the vehicle does not behave as efficiently as a regular airfoil in creating lift. This brings us to the final conclusion that cambering in this model vehicle does not create a significant enough effect to reduce drag as described in section 2.1 and can thus not be used to increase performance in the WSC.

A note has to be made about the method of determining errors in this thesis, they do not tolerate the asymmetry seen in the symmetric vehicle's drag profile in figure 4.6 and do not include the possibility of the symmetric vehicle's side force at a 0-degree angle of attack to be zero. This uncertainty in symmetric values can be contributed to the unstructured discretization of the fluid domain, which results in an asymmetric mesh. Because the errors do not capture the uncertainties seen in the results, the method used to estimate the error is incorrect or has not been done correctly. In future studies, more care should be taken into the effect of an asymmetric mesh, and the determination of errors. However, the trends that are observed in the drag profiles of cambered vehicles, are closely similar to the predicted profiles, which gives confidence in the conclusions that can be drawn from the results.

Regardless of the results for cambering SEVs, the possibility to optimize in an asymmetric wind distribution remains. The results in figure 4.6 suggest that an asymmetric drag distribution is achievable, only a better method of introducing asymmetry than the one presented in this thesis is required. The principle by which drag could be reduced has only been disproven for this specific SEV model. A model where airfoil profiles are more prevalent, such as the Brunel Solar Team's Nuna[22], might result in more promising results. However, the application on an existing vehicle is not required, there might be more to learn from a simplistic SEV design.

References

[1] Bridgestone World Solar Challnege. *World Solar Challenge*. www.worldsolarchallenge.org. URL: https://www.worldsolarchallenge.org/.

[2] Top Dutch Solar Racing. *Top Dutch Solar Racing*. solarracing.nl. URL: https://solarracing.nl/.

[3] Bob Allen. *NACA Airfoils*. nasa.com, 2011. URL: https://www.nasa.gov/image-feature/langley/100/naca-airfoils.

[4] S. J. Hulshoff. *Airfoil Coordinate Database*. Tudelft.nl, 2012. URL: https://aerodynamics.lr.tudelft.nl/cgi-bin/afCDb.

[5] *Airfoil Tools*. airfoiltools.com, 2019. URL: http://airfoiltools.com/.

[6] Tjitte van der Ploeg. "Modeling of a solar powered vehicle". PhD thesis. Jan. 2020, pp. 25–31.

[7] R. J. Adrian, K. T. Christensen, and Z.-C. Liu. "Analysis and interpretation of instantaneous turbulent velocity fields". In: *Experiments in Fluids* 29 (Sept. 2000), pp. 275–290. DOI: 10.1007/s003489900087.

[8] J. Boussinesq. "Démonstration générale de la construction des rayons lumineux par les surfaces d'onde courbes". In: *Journal de Physique Théorique et Appliquée* 2 (1903), pp. 10–14. DOI: 10.1051/jphystap:01903002001001.

[9] David C. Wilcox. "Formulation of the k-w Turbulence Model Revisited". In: *AIAA Journal* 46 (Nov. 2008), pp. 2823–2838. DOI: 10.2514/1.36541.

[10] Ansys. *ANSYS FLUENT 12.0 Theory Guide - 4.5.2 Shear-Stress Transport (SST) - Model*. afs.nea.it, 2021. URL: https://www.afs.enea.it/project/neptunius/docs/fluent/html/th/node67.htm.

[11] T.J. Craft, Brain Launder, and K. Suga. "Development and Application of a Cubic Eddy-Viscosity Model of Turbulence". In: *International Journal of Heat and Fluid Flow* 17 (Apr. 1996). DOI: 10.1016/0142-727X(95)00079-6.

[12] Ansys. *ANSYS Fluent Software — CFD Simulation*. ansys.com, 2017. URL: https://www.ansys.com/products/fluids/ansys-fluent.

[13] Aeronautical Engineer Hermann Schlichting. *Boundary Layer Theory, etc.* Pergamon Press: London; Verlag G. Braun: Karlsruhe; Karlsruhe Printed, 1955.

[14] Patrick J. Roache. "Verification and Validation in Fluids Engineering: Some Current Issues". In: *Journal of Fluids Engineering* 138 (Aug. 2016). DOI: 10.1115/1.4033979.

[15] J. W. Slater. *Examining Spatial (Grid) Convergence*. www.grc.nasa.gov, Feb. 2021. URL: https://www.grc.nasa.gov/www/wind/valid/tutorial/spatconv.html.

[16] J D Anderson. *Fundamentals of aerodynamics*. Mcgraw-Hill Publishing Co, 2007.

[17] Ansys. *ANSYS Fluent Mosaic Technology Automatically Combines Disparate Meshes with Polyhedral Elements for Fast, Accurate Flow Resolution*. Ansys.com, 2020. URL: https://www.ansys.com/content/dam/resource-center/white-paper/ansys-fluent-mosaic-technology-wp.pdf.

[18] Jiyuan Tu, Guan-Heng Yeoh, and Chaoqun Liu. "Chapter 7 - Practical Guidelines for CFD Simulation and Analysis". In: *Computational Fluid Dynamics (Third Edition)*. Ed. by Jiyuan Tu, Guan-Heng Yeoh, and Chaoqun Liu. Third Edition. Butterworth-Heinemann, 2018, pp. 255–290. ISBN: 978-0-08-101127-0. DOI: https://doi.org/10.1016/B978-0-08-101127-0.00007-6. URL: https://www.sciencedirect.com/science/article/pii/B9780081011270000076.

[19] *Air - Thermophysical Properties*. Engineeringtoolbox.com, 2019. URL: https://www.engineeringtoolbox.com/air-properties-d_156.html.

[20] Rhinoceros. *Rhinoceros*. Rhino3d.com, 2019. URL: https://www.rhino3d.com/.

[21] Meteoblue. *Meteoblue*. Meteoblue.com, 2019. URL: https://www.meteoblue.com/.

[22] Brunel Solar Team. *Brunel Solar Team*. brunelsolarteam.com. URL: https://brunelsolarteam.com/.